Received 11 October 2025; accepted 2 December 2025. Date of publication 11 December 2025; date of current version 9 February 2026.

Digital Object Identifier 10.1109/OJAP.2025.3643633

On the Synthesis of Aperiodic Multi-Atom 1-Bit Reconfigurable Passive EMSs at 140 GHz

TAEYOUNG KIM [1,2] (Member, IEEE), FRANCESCO ZARDI [3] (Member, IEEE), SANGMIN LEE [1] (Graduate Student Member, IEEE), JINHYUN KIM [4] (Graduate Student Member, IEEE), UICHAN PARK [4] (Graduate Student Member, IEEE), JUNGSUEK OH [4] (Senior Member, IEEE), SANGJO CHOI [1] (Member, IEEE), AND GIACOMO OLIVERI [3] (Fellow, IEEE)

[1]The School of Electronic and Electrical Engineering, Kyungpook National University, Daegu 41566, South Korea
[2]R&D Division, Korea Defense Industry, Daejeon 34062, South Korea
[3]Department of Civil, Environmental, and Mechanical Engineering (DICAM), University of Trento, 38123 Trento, Italy
[4]Department of Electrical and Computer Engineering, Seoul National University, Seoul 08826, South Korea

CORRESPONDING AUTHOR: SANGJO CHOI (e-mail: sangjoc@knu.ac.kr)

This work was supported in part by the Korea Government Ministry of Science and ICT (MSIT) under Grant 2021-0-00763 and in part by the European Union through NextGenerationEU, including the ICSC National Centre for HPC under Grant CUP: E63C22000970007, INSIDE-NEXT under Grant CUP: E53D23000990001, AURORA under Grant CUP: E53D23014760001, Telecommunications of the Future under Grant CUP: D43C22003080001, and the DICAM-EXC Project under Grant CUP: E63C22003880001, funded by the Italian Ministry of Education, Universities, and Research.

ABSTRACT An innovative reconfigurable passive electromagnetic skin (RP-EMS) architecture is proposed to support a single reflection beam while suppressing undesired beams, using 1-bit switching with minimal hardware complexity. The architecture is the first to simultaneously optimize the meta-atom arrangement and their 1-bit switching descriptors using the integer-coded evolutionary algorithm, supporting multiple reflection scenarios. The process yields one aperiodic meta-atom arrangement that effectively mitigates periodic phase quantization errors typical of 1-bit RP-EMS layouts, while changing reflection angles solely through 1-bit switching. An aperture-coupled patch-based meta-atom topology with well-separated and linearized phase responses is employed to enable 1-bit switching using a short/open connection. As a proof of concept, 30×30 RP-EMS prototypes with a 3.14×3.14 cm^2 aperture and $\lambda/2$ periodicity at 140 GHz are designed and fabricated, demonstrating reflection at 15°, 30°, and 45° under normal incidence. The prototypes exhibited robust beam steering with QLL consistently below -10 dB and SLL up to -10 dB, confirming the effectiveness of the proposed MASB layout. In addition, the structures achieve 3-dB gain bandwidth exceeding 11% and high reflection efficiencies over 15%, referenced to a conductor surface of the same size. These results validate the potential of the proposed architecture for implementing multi-functional 1-bit RP-EMS with controlled sidelobes and no grating lobe near 140 GHz.

INDEX TERMS Electromagnetic skins (EMSs), reconfigurable intelligent surfaces (RIS), smart EM environment (SEME), multi-atom skin (MA), surface electromagnetics, next-generation communications.

I. INTRODUCTION

THE development of inexpensive and reliable Reconfigurable-Passive Electromagnetic Skins (RP-EMSs), also labeled as Reconfigurable Intelligent Surfaces (RIS), represents one of the key pillars in the implementation of next generation communication systems based on the Smart Electromagnetic Environment (SEME) paradigm [1], [2], [3], [4], [5], [6]. Thanks to their advanced wave manipulation capabilities, RP-EMS allow the wireless propagation to be tailored in real time according to the network quality-of-service objectives and needs, hence effectively enabling the transition of environments from their traditional "propagation-hostile" role to a user-controllable one [1], [2], [5], [6]. This is accomplished thanks to the possibility to control the local reflection coefficients of RP-EMSs by electronically acting on their atomic properties.

Unfortunately, achieving such performance can require expensive architectures and control strategies, especially if multi-bit-atoms are at hand [5], [6]. To enable the exploitation of such a technology while mitigating cost issues, single-bit RIS designs have been proposed in the literature [2], [5], [7], [8], [9], [10]. However, single-bit designs generally suffer from a limited reflected wave control owing to the considerable quantization error introduced on the supported surface currents [5], [11]. This usually results in high quantization lobes, poor sidelobe control, and reduced power focusing efficiency [2], [5], [11].

This work proposes an innovative single-bit RP EMS inspired by randomly pre-phased single-bit meta-atoms [12], [13], [14], [15] to overcome such issues. The pre-phased method optimizes the combination of meta-atoms using an array factor formula that relies solely on phase adjustments for beam control and randomization. Hence, surface current modeling for the meta-atoms has not been implemented. In contrast, this study introduces a novel approach to address the same issue by modeling different single-bit meta-atoms, referred to as Multi-Atom Single-Bit (MASB) units using surface current. Each MASB unit supports a single-bit reconfiguration across multiple phase profiles directly identify the optimized aperiodic combination of the unit cells for targeted reflection scenarios. It is noted that unit cell positions are distributed in a periodic grid, while only their phase profiles are configured in an aperiodic way. In principle, this architecture can enable (i) more accurate surface current control, while (ii) yielding control and fabrication costs analogous to a single-bit RP-EMS [2]. Nevertheless, the design and implementation of the resulting MASB skin feature some unique challenges and difficulties. More in detail:

- the design of the M classes of atoms to be included in the architecture requires careful modeling and optimization, which is usually carried out according to the local periodicity approximation [1], [2], [3], [4], [5], [6]. Since the different classes of meta-atoms are then combined in an aperiodic fashion, this can result in a non-negligible approximation that may cause a degradation of the overall reflection properties. To overcome such issue, the introduced M meta-atoms should have low interelement coupling and excellent phase linearity while also supporting well-separated phase responses;
- unlike both static-passive EMSs (SP-EMSs) [16], [17], [18] and RP-EMSs [2], the synthesis of the skin arrangement turns out a hybrid problem where the descriptors are partially static (i.e., the choice of the meta-atom among the M available designs to be located in a certain position) and partially dynamic (i.e., the definition of each meta-atom's ON/OFF configuration at the micro-scale level to afford a set of N different macro-scale functionalities). As such, no state-of-the-art technique can be straightforwardly adopted in the MASB design process, and random search approaches [12], [13], [14], [15] can provide sub-optimal quantization lobe control.

Following such considerations, an innovative design/control approach is proposed hereinafter for the synthesis of MASB reconfigurable skins. More specifically, starting from the definition of N functionalities that the skin will have to support (e.g., different anomalous wave reflections), the MASB architecture and corresponding Meta Atom (MA) setups will be synthesized as a trade-off solution to guarantee the best sidelobe control in the N different operative conditions. To this end, and unlike [12], [13], [14], [15], an integer-coded evolutionary algorithm inspired by genetic operators [19] will be customized to the scenario at hand. To demonstrate the features and potentialities of the arising concept and the introduced synthesis method, the design and implementation of a set of MASB EMSs operating at 140 GHz will be demonstrated. To this end, an aperture-coupled patch-based meta-atom architecture simultaneously guaranteeing M different geometries with similar physical architecture but supporting well-separated and linearized phase responses is introduced. The reconfigurability of the single-bit switching was implemented both with and without a physical connection in the coupled transmission line in the unit cell. This implementation effectively replicates typical electronic single-bit switching using diodes and was adapted as proof of concept at such a high frequency. A set of numerical and experimental results at 140 GHz will be shown to illustrate the feasibility of the proposed architecture and the effectiveness of the resulting control strategy in terms of sidelobe mitigation and grating lobes elimination.

Accordingly, the main innovative contributions of this work, to the best of the authorsâ^{TM} knowledge, include: (i) the development of an innovative optimization approach that enables the simultaneous design of both the trade-off combination of meta-atom topology to achieve desired reconfigurability and the electronic setup of each meta-atom under N different reflection conditions; (ii) the demonstration of a feasible architecture for a class of simplified meta-atoms supporting M different phase configurations operating at 140 GHz with excellent phase linearity and minimal interelement coupling; and (iii) the full-wave numerical and experimental validation of the potential to achieve multi-functional single-bit RP-EMS with well-controlled sidelobes and no grating lobe.

The paper is organized as follows. After the formulation and solution process of the design and control problem (Section II), the synthesis of a set of single-bit 140 GHz meta-atom architectures supporting different reflection phase values will be illustrated together with the MASB design and control process (Section III). The results of the experimental validation carried out at 140 GHz will be shown next (Section IV), before concluding (Section V).

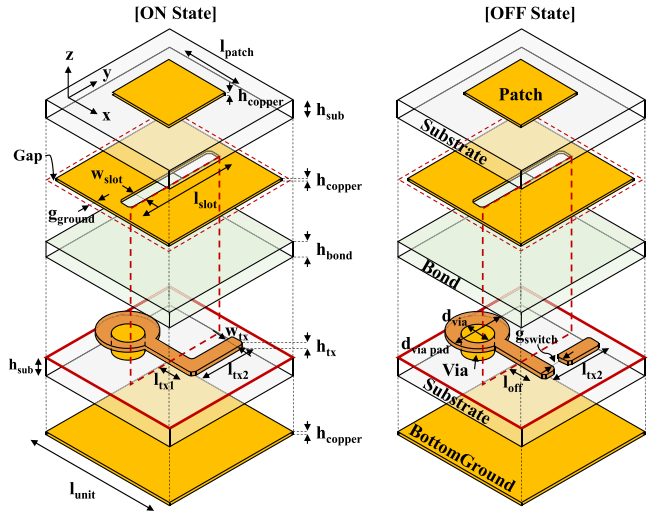

FIGURE 1. Exploded view of the proposed Meta Atom with ON/OFF.

II. MASB DESIGN PROBLEM AND SOLUTION PROCESS

Let us consider an arrangement of $P \times Q$ reconfigurable passive meta-atoms which are illuminated by a primary transverse-electric (TE) polarized source generating an incident field $\mathbf{E}_{inc}(\mathbf{r}) = E_{inc}(\mathbf{r})\widehat{\upsilon}$.[1] Let us assume that the topology of each meta-atom can be selected from a set of M available cells, each one enabling a single bit reconfiguration. Under the local periodicity approximation and exploiting the Love's equivalence theorem, the magnitude of the far-field reflected by such a structure can be derived as discussed in [6], [16], [18], [20] by (i) discretizing the surface current according to the identified $P \times Q$ grid, (ii) associating to each unit cell the complex local TE reflection coefficient which can be computed numerically (e.g., using full-wave solvers) as the scattering coefficient of the first-order Floquet mode, (iii) approximating the surface electric and magnetic currents as uniformly distributed in the pq-th cell, and (iv) computing the radiated field from the resulting discretized current distribution exploiting free-space Green's function, as detailed in [20]. According to such a formulation, the following equation holds true (see [16], [18], [20]).

$$|\mathbf{E}_{ref}(\theta,\varphi;\underline{A},\underline{C})|^2 = \zeta(\theta,\varphi) \times |\sum_{p=1}^{P}\sum_{q=1}^{Q}\Gamma(a_{pq},c_{pq}) E_{inc}(\mathbf{r}_{pq}) \exp[jk(x_p \sin\theta\cos\varphi + y_q \sin\theta\sin\varphi)]|^2 \quad (1)$$

where $\zeta(\theta,\varphi) = \frac{k^2 \mathrm{sinc}^2(\frac{k\Delta_x \sin\theta\cos\varphi}{2})\mathrm{sinc}^2(\frac{k\Delta_y \sin\theta\sin\varphi}{2})}{2\eta} |\widehat{\upsilon}\cdot\widehat{\mathbf{x}}\sin\theta\cos\varphi + \widehat{\upsilon}\cdot\widehat{\mathbf{y}}\sin\theta\sin\varphi|^2$, k and η are the free-space wavenumber and characteristic impedance, respectively, $\Delta_x \times \Delta_y$ is the meta-atom lattice periodicity, $\mathbf{r}_{pq} = (x_p, y_q)$ is the barycenter of the pq-th cell, and $\Gamma(a_{pq}, c_{pq})$ is the TE complex local reflection coefficient in the pq-th cell. As for this latter, its value is controlled by

- the topology $a_{pq} \in \{1,\ldots,M\}$ of the meta-atom selected for the pq-th cell among the available M classes of atoms for the design at hand. It is worth remarking that $\underline{A} = \{a_{pq}; p = 1,\ldots,P, q = 1,\ldots,Q\}$ encodes the geometrical/physical properties of the MASB layout, and it cannot be modified after fabrication;
- the electronic configuration $c_{pq} \in \{0,1\}$ of the pq-th single-bit meta-atom. It can be noticed that $\underline{C} = \{c_{pq}; p = 1,\ldots,P, q = 1,\ldots,Q\}$ encodes the electronic configuration properties of the MASB layout, and it can be dynamically modified to adapt the skin reflection properties.

Accordingly, the problem of synthesizing a MASB design capable of supporting N independent user-defined wave manipulation functionalities (i.e., $|\widehat{\mathbf{E}}^n_{ref}(\theta,\varphi)|^2$, $n = 1,\ldots,N$, different target fields) can be formulated as that of synthesizing the optimal layout configuration $\underline{A}^{opt}$ and the corresponding N electronic setups $\mathcal{C}^{opt} = \{\underline{C}_n^{opt}, n = 1,..,N\}$ so that

$$\Phi(\underline{A},\mathcal{C}) = \sum_{n=1}^{N}\iint\left(|\widehat{\mathbf{E}}^n_{ref}(\theta,\varphi)|^2 - |\mathbf{E}_{ref}(\theta,\varphi;\underline{A},\underline{C}_n)|^2\right)\mathrm{d}\theta\mathrm{d}\varphi \quad (2)$$

is minimized.

According to the previous discussion, the solution of the MASB design problem requires to address two separate sub-tasks, that is (i) the definition of the M single-bit MA topologies capable of supporting the desired reflection coefficient control (i.e., each meta-atom configuration has to allow switching $\angle\Gamma$ between 2 different values by operating on the associated configuration bit), and (ii) the optimization of the layout descriptors $\underline{A}$, $\mathcal{C}$.

As for the former sub-task, a parametric approach is adopted in the following that, starting from a reference geometry (Fig. 1), enables the derivation of M cells maximizing the overall phase coverage, that is complying with $\angle\Gamma(m,0) - \angle\Gamma(m,1) \approx 180\hat{A}°$, $m = 1,\ldots,M$, and with $\angle\Gamma(m,0) - \angle\Gamma(m+1,0) \approx \frac{180°}{M}$, $m = 1,\ldots,M-1$ (Section III-A).

With reference to the layout synthesis, an evolutionary optimization-inspired strategy [2], [19] is customized in the following. More in detail, an iterative strategy is implemented in which, at each iteration $v = 1,\ldots,V$, a set of L candidate solutions $\{\underline{A}_l^v, \mathcal{C}_l^v\}$, $l = 1,\ldots,L$ are generated through a succession of Genetic operators (*mutation, crossover, selection*) [19] until either the maximum number of iterations is achieved (i.e., $v = V$) or a convergence condition concerning the resulting cost function is satisfied. Such a choice is motivated by the fact that unlike SP-EMSs [17], [18], the solution descriptors are discrete in nature. Moreover, the cost function turns out highly nonlinear, also owing to the need of matching multiple target fields with a single architecture [Eq. (2)]. Furthermore, the number of degrees-of-freedom (DoFs) turns out much larger with respect to a standard single-atom RP-EMS with

[1] A single polarization is considered hereinafter for the sake of notation simplicity. However, the tensorial formulation can be derived by following [18].

TABLE 1. Meta atom design - unit cell descriptors.

Common Parameter Values (mm)					
l_{patch}	0.49	l_{slot}	0.77	w_{slot}	0.10
g_{ground}	0.05	w_{tx}	0.10	g_{switch}	0.10
d_{via}	0.20	$d_{\text{via pad}}$	0.40	h_{copper}	0.018
h_{sub}	0.127	h_{bond}	0.07	h_{tx}	0.03

TABLE 2. Meta atom transmission line parameters.

MA State	l_{tx1} (mm)	l_{tx2} (mm)	l_{off} (mm)
MA-0 [ON]	0.36	–	–
MA-0 [OFF]	0.36	–	0.00
MA-1 [ON]	0.29	0.48	–
MA-1 [OFF]	0.29	0.48	0.29
MA-2 [ON]	0.41	0.26	–
MA-2 [OFF]	0.41	0.26	0.21
MA-3 [ON]	0.31	0.28	–
MA-3 [OFF]	0.31	0.28	0.11

the same aperture [2], since the design must be carried out simultaneously optimizing the meta-atom arrangement (i.e., $P \times Q$ integer DoFs) as well as the N electronic configurations (i.e., $P \times Q \times N$ binary DoFs).

It is worth remarking that such differences with respect to state-of-the-art problems have a direct impact on the adopted methodological choices. In fact, the proposed technique aims at the simultaneous optimization of both the meta-atom topology distribution and of their electronic descriptors in N different operative conditions, unlike state-of-the-art approaches for the design/control of RP-EMSs [2] (only devoted to the electronic setup of arrangements of identical atoms) or SP-EMSs [17] (only aimed at the geometrical configuration of each meta-atom, without taking into account any reconfigurability).

III. MASB DESIGN AND NUMERICAL VALIDATION

A. META ATOM DESIGN AND DESCRIPTORS

The first step of the design consists of the definition of a MA topology supporting M different MAs that will have to be combined in the MASB arrangement. To this end, a MA topology based on an aperture-coupled patch has been adopted (Fig. 1) [21], [22], [23]. A set of $M = 4$ MASB MAs has been designed to operate at 140 GHz so that, according to the formulation illustrated in Section II, each one enables a phase separation of $\approx \frac{180^\circ}{M} = 45^\circ$, $m = 1, \ldots, M-1$ with respect to the previous configuration. More specifically, the introduced MA architecture consists of a total of four metal layers that feature (reading the architecture from the top) a square patch, a slotted ground with a gap, a transmission line ("Tx line"), and a bottom ground plane (Fig. 1), following the PCB stack-up used in [15].

The MA, designed for x-polarized excitation, was parametrically optimized to ensure the desired Γ performance. More in detail, lattice spacing of 1.07 mm (l_{unit}), corresponding to half-wavelength at 140 GHz, has been adopted. Each metal layer of the MA with height of 0.018 mm (h_{copper}) has been patterned using PCB processing with two TLY-5 substrates ($\tan\delta = 0.0009$ and $\varepsilon_r = 2.2$). The two substrates with height of 0.127 mm (h_{sub}), each designed separately, were stacked using two Taconic bond sheets of 40 μm thickness ($\tan\delta = 0.0025$ and $\varepsilon_r = 2.35$), thus resulting in a separation of 70 μm (h_{bond}) after melting and compression. The designed MA has been modeled and simulated using Ansys HFSS under the local periodicity approximation [17] (i.e., exploiting periodic boundary conditions and Floquet port configurations). A single-bit switching was implemented employing a short/open-circuit connection with and without a physical connection in the coupled transmission line, respectively, as shown in Fig. 1. The dimensions for the patch, slot, and Tx lines were parameterized by l_{patch}, l_{slot}, w_{slot}, l_{tx1}, l_{tx2}, w_{tx}, and g_{switch}, respectively. The common geometrical descriptors of optimized layouts with the $M = 4$ are resumed in Tab. 1, while the features differentiating the meta-atoms within the derived class are provided in Tab. 2.

It is worth remarking that, to mitigate mutual coupling effects between adjacent units and guarantee more stable performance over wider scattering angles, the starting point of the Tx line has been connected to the bottom ground through a via with a diameter of 0.2 mm (d_{via}) (Fig. 1). Additionally, for a stable via connection, a via pad with a diameter of 0.4 mm ($d_{\text{via pad}}$) is inserted, and the height of the Tx line is increased by plating with 0.012 mm copper, making it higher than the other layers, resulting in a total height of 0.03 mm (h_{tx}). Such a configuration enables the reduction of the electric field of the Tx line that travels to nearby cells thanks to the shorting with the ground. Moreover, a gap ($g_{\text{ground}} = 0.05$ mm) around the four sides of the slotted ground has been introduced in the second layer to prevent the surface current generated by the Tx line from flowing to adjacent MAs.

B. PHASE LINEARIZATION THROUGH TRANSMISSION LINE LENGTH PARAMETRIC ANALYSIS

In the frequency range above 100 GHz, where the size of the MA reduces to a few millimeters, even marginal deviations in the structure can significantly alter the characteristics of the MA. To reduce and linearize the Γ phase discrepancy due to the fabrication offsets in the metallic lines, the reflection coefficient phase variations have been adjusted by parametrically analyzing their dependency on the transmission line length [22], [23].

To this end, the length of the slot (l_{slot}) has been set 0.77 mm so that it is slightly longer than half the wavelength of the guided field (i.e., $\lambda_g = 1.42$ mm) to induce strong coupling as the Tx line passes through the center of the

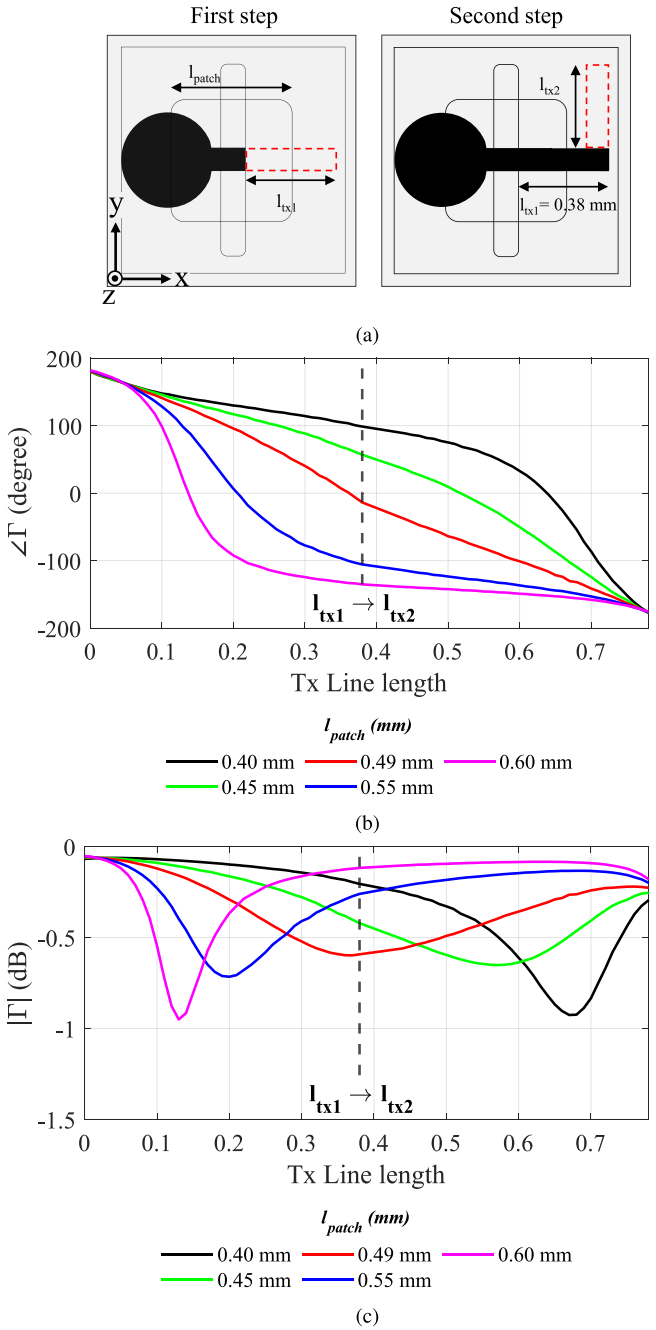

FIGURE 2. (a) Simulation analysis procedure. Parametric analysis of the (b) phase and (c) magnitude of the reflection coefficient at 140 GHz as a function of the line length, for different patch side values l_{patch}.

slot. The variations in the phase and magnitude of Γ have been then analyzed as a function of Tx line length for $l_{\text{patch}} \in \{0.40, 0.45, 0.49, 0.55, 0.60\}$ mm under broadside illumination conditions. The plots of the phase [Fig. 2(b)] and magnitude [Fig. 2(c)] of the reflection coefficient for different l_{patch} values when varying the Tx line length are shown in Fig. 2.

To perform this parametric analysis, the Tx line length l_{tx1} was initially increased from 0 to 0.38 mm while maintaining a fixed l_{patch} in the ON state of the Meta-Atom [left inset in Fig. 2(a)]. Afterward, l_{tx1} was kept fixed at 0.38 mm, and the length of the bent section, denoted as l_{tx2}, was extended from 0 to 0.40 mm to further elongate the Tx line [right inset of Fig. 2(a)]. This process resulted in a cumulative variation of 0.78 mm in the total length of the Tx line.

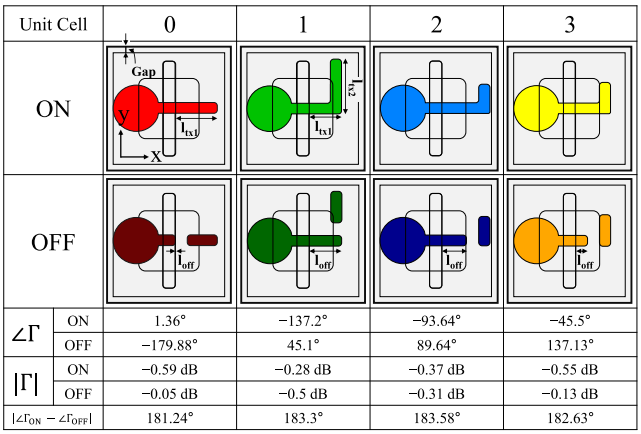

		0	1	2	3
∠Γ	ON	1.36°	−137.2°	−93.64°	−45.5°
	OFF	−179.88°	45.1°	89.64°	137.13°
|Γ|	ON	−0.59 dB	−0.28 dB	−0.37 dB	−0.55 dB
	OFF	−0.05 dB	−0.5 dB	−0.31 dB	−0.13 dB
$\lvert\angle\Gamma_{ON} - \angle\Gamma_{OFF}\rvert$		181.24°	183.3°	183.58°	182.63°

FIGURE 3. Optimized layouts of 1-bit MA structures ($M = 4$) and associated reflection coefficient properties at 140 GHz.

Fig. 2(b) indicates that the Tx line length of 0.78mm ($\approx \lambda_g/2$) is required to cover a 360° phase shift (approximately $2\beta_g l_{\text{max}}$) for all l_{patch}. In particular, in $l_{\text{patch}} = 0.49$ mm, the slope of the phase variation closely follows $2\beta_g$, resulting in a linear phase variation of $2\beta_g l$ for a $\frac{\lambda_g}{2}$-long Tx line. Such a reflection phase variation exhibits a behavior similar to that of an ideal microstrip line with a dielectric constant ($\varepsilon_r = 2.2$) at 140 GHz. Therefore, we set the optimal l_{patch} to 0.49 mm, which induces the most linear phase variation with respect to changes in the Tx line.

Fig. 2(c) shows that as l_{patch} approaches 0.49 mm, the |Γ| magnitude becomes increasingly stable at 140 GHz with a variation within 0.6 dB, indicating a well-matched coupling between the patch and Tx line induced by the slot. Therefore, such linearized phase variation structures can alleviate performance degradation caused by manufacturing errors, as they exhibit greater robustness against fabrication tolerances in high-frequency PCB processes. This linearization step resulted in different values for l_{patch}, l_{slot}, l_{tx1}, and l_{tx2} compared to those used in the unit cells of the same PCB stack-up [15].

Fig. 3 presents the final design of $M = 4$ pairs of 1-bit MAs. The slotted ground in the second layer has a gap ($g_{\text{ground}} = 0.05$ mm), and to control Γ value in the ON state of the MA, we adjusted the lengths of l_{tx1} and l_{tx2} to achieve ∠Γ close to −135°, −90°, −45°, and 0°. Similarly, to control the Γ value in the OFF state, we adjusted the length of l_{off} to achieve phase angles close to 45°, 90°, 135°, and 180°. Since all parameters of the structure are well-matched at 140 GHz, |Γ| of the designed four pairs of MAs is maintained at −0.59 dB or lower, ensuring low reflection losses.

Finally, Fig. 4 depicts the simulated reflection coefficient of the MA from 120 to 160 GHz. At 140 GHz, the

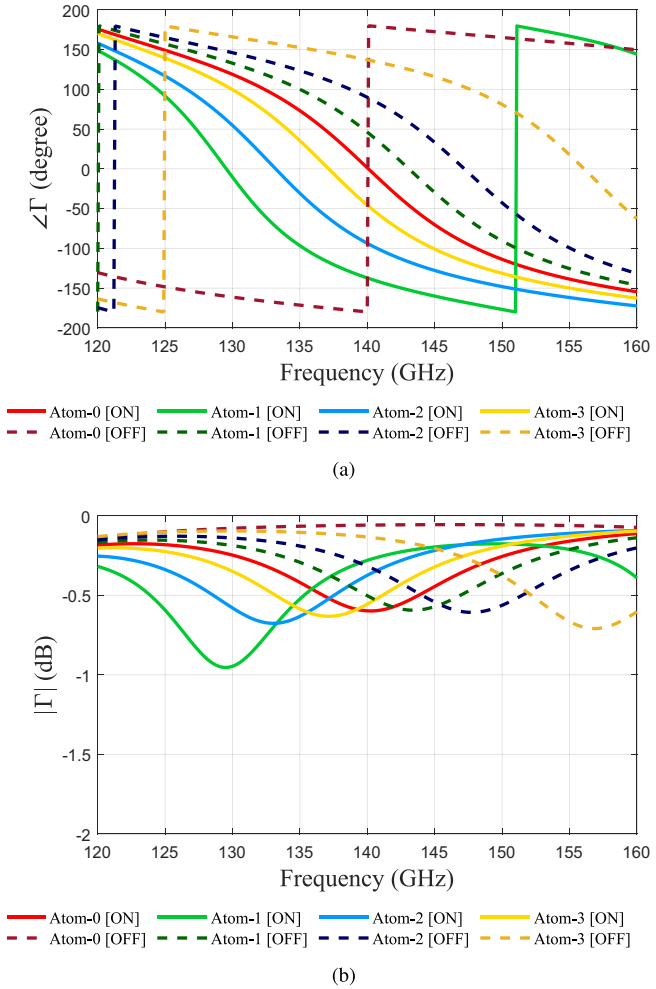

FIGURE 4. Full-wave simulated (a) reflection phase ($\angle\Gamma$) and (b) magnitude ($|\Gamma|$) of the optimized MAs with $M = 4$ across the frequency range of 120–160 GHz under normal incidence.

MA maintains a phase difference between the different meta-atoms of approximately 45°, as desired [Fig. 4(a)]. Additionally, the designed MA exhibits $|\Gamma| > -1$ dB across the entire frequency range [Fig. 4(b)]. This can be attributed to the wide bandwidth characteristic of the aperture-coupled patch structure.

C. MASB LAYOUT DESIGN AND FULL-WAVE VALIDATION

The MASB design process illustrated in Section II is employed next to demonstrate the possibility to achieve desired reconfiguration capabilities. Towards this end, the design of a $P \times Q = 30 \times 30$ layout has been carried out assuming a time-harmonic plane wave illuminating the layout from broadside direction at 140 GHz. The synthesis has been performed assuming that $N = 3$ different functionalities must be supported by the MASB layout and setting the target reflected fields $|\widehat{\mathbf{E}}^n_{ref}(\theta, \varphi))|^2$, $n = 1, .., N$ so that they corresponds to an anomalous coherent reflection towards $N = 3$ different directions (i.e., $\widehat{\theta}^n \in \{15°, 30°, 45°\}$). Note that the target reflected fields are

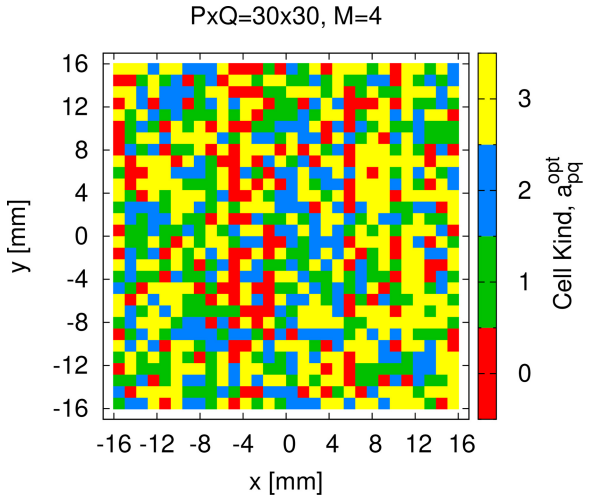

FIGURE 5. Optimized meta atom configuration $\underline{A}^{opt}$ with $P \times Q = 30 \times 30$.

normalized radiation patterns of the uniform array at each steering angle. As for the design process, the evolutionary optimization configuration has been implemented according to state-of-the-art guidelines [19] by setting $V = 1000$, $L = 100$, the mutation probability to 0.02, and the cross-over probability to 0.6.

The optimized meta-atom configuration $\underline{A}^{opt}$ and the corresponding N electronic setups $\mathcal{C}^{opt} = \{\underline{C}^{opt}_n, n = 1, .., N\}$ are shown in Fig. 5 and Fig. 6, respectively. As it can be noticed, the optimal layout to support the $N = 3$ functionalities turns out aperiodic, as theoretically expected (Fig. 5). In fact, such a feature, which indirectly guarantees quantization errors to be aperiodically distributed across the aperture, is required to avoid the presence of grating lobes and potentially mitigate the presence of major sidelobes. To quantify this effect, the phase quantization error for the mn-th element can be expressed as

$$\Delta\phi_{mn} = \phi_{mn} - \phi^{\text{req}}_{mn} \tag{3}$$

where ϕ_{mn} is the implemented phase state on the mn-th element and ϕ^{req}_{mn} is the required discretized phase on the mn-th element based on continuous phases for accurate reflection angle [11]. In the conventional 1-bit EMS, only two states (0° and 180°) for ϕ_{mn} are available, so $\Delta\phi_{mn}$ takes on periodic values across the aperture, which give rise to quantization lobes. By contrast, in the proposed MASB configuration, the errors should be distributed aperiodically, similar to Fig. 6, leading to the suppression of quantization lobes.

Such an aperiodicity is confirmed in the corresponding optimized statuses (Fig. 6). Moreover, the plots of the electronic configuration for the different reflection angles shows the benefit of exploiting multiple single-bit atoms in the same structure, since a considerable surface response variability can be achieved despite each MA enabling only an ON/OFF reconfiguration (Fig. 6).

The model of the resulting architecture is shown in Fig. 7. The HFSS-simulated $|\mathbf{E}_{ref}(\theta, \varphi; \underline{A}^{opt}, \underline{C}^{opt}_n)|^2$ are analyzed

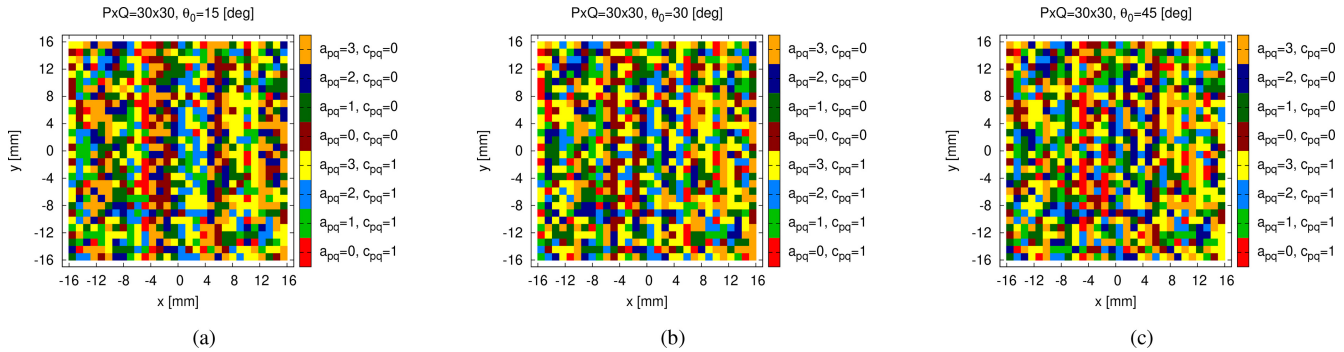

FIGURE 6. Optimized meta-atom electronic setup (C_n^{opt}) for (a) $n = 1$ ($\hat{\theta}^n = 15°$), (b) $n = 2$ ($\hat{\theta}^n = 30°$), and (c) $n = 3$ ($\hat{\theta}^n = 45°$) functionalities under normal incidence.

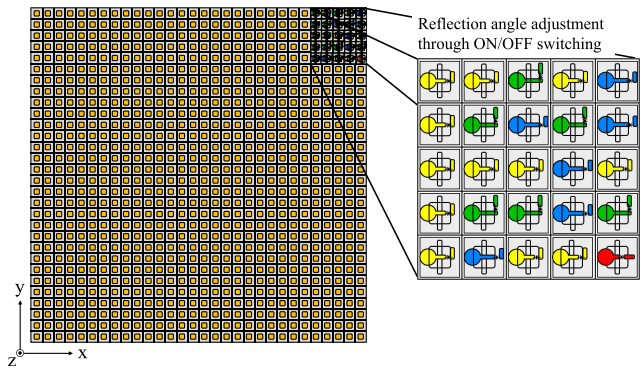

FIGURE 7. HFSS Modeling of the $P \times Q = 30 \times 30$ 1-bit MASB EMS with ON/OFF switching.

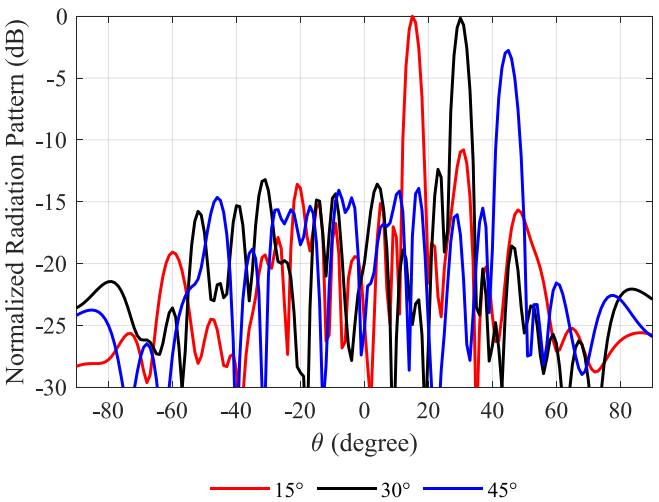

FIGURE 8. HFSS-simulated patterns in the $\phi = 90°$-plane for the $n = 1$ ($\hat{\theta}^n = 15°$), $n = 2$ ($\hat{\theta}^n = 30°$), and $n = 3$ ($\hat{\theta}^n = 45°$) functionalities under normal incidence.

next for the $N = 3$ designed functionalities to assess the achievable reflection capabilities and sidelobe control when accounting for the approximations resulting from the aperiodic coupling between the cells and truncation effects (Fig. 8). The plots of the far-field reflected pattern in the $\varphi = 90°$ cut show that (i) despite the exploitation of single-bit MAs, no grating lobe appears regardless of the reflection angle (Fig. 8), and (ii) the sidelobes turn out to be well controlled in all operative conditions, hence demonstrating that quantization errors are well mitigated by the proposed MASB concept. More specifically, the peak sidelobe level (SLL) in the different configuration statuses (i.e., according to Fig. 8) turns out to be $SLL|_{\widehat{\theta}^n=15°} = -10.80$ dB, $SLL|_{\widehat{\theta}^n=30°} = -12.22$ dB, and $SLL|_{\widehat{\theta}^n=45°} = -11.16$ dB (Fig. 8). Additionally, the specular quantization lobe level (QLL: $|\mathbf{E}_{ref}(\theta \approx -\widehat{\theta}^n, \varphi_r; \underline{A}^{opt}, \underline{C}_n^{opt})|^2 - |\mathbf{E}_{ref}(\theta = \widehat{\theta}^n, \varphi_r; \underline{A}^{opt}, \underline{C}_n^{opt})|^2$) decreased by -15.17, -13.05, and -11.89 dB at $\widehat{\theta}^n = 15°$, 30°, and 45°, respectively, if compared to a standard 1-bit architecture which would present QLL = 0 [dB] by definition (Fig. 8).

These numerical results turn out even more interesting taking into account that the SLL performance of a skin with ideal phase control (i.e., no quantization and perfect matching of the reference pattern) would be ≈ -13.5 dB. Such a result shows that, beyond avoiding grating lobes, the MASB concept can be effectively employed to yield controlled sidelobes of RP-EMSs (i.e., less than 3-dB away from an ideal skin with infinite bits of the same size) with minimum hardware control (i.e., only $P \times Q$ diodes and corresponding biasing lines). As a trade-off, the absolute reflected power at each reflection angle is approximately 3-dB lower than that of the typical 1-bit EMS, because the optimization matched normalized patterns and did not constrain absolute gain in the cost function. Although such beam-shaping optimization can inherently reduce gain, future work will incorporate gain constraints to reduce this gap. To assess the frequency stability of the proposed EMS, we performed additional 3D full-wave simulations at 137 GHz, 140 GHz, and 142 GHz for a representative steering angle of 30°. The corresponding radiation patterns in the u-v plane are provided in Fig. 9. At the center frequency of 140 GHz, the main beam is sharply focused with low sidelobes and no quantization lobes. At 137 GHz and 142 GHz, the main-beam direction remains stable, although sidelobe levels near broadside increase up to near -9 dB, a similar level to the other maximum SLLs. Tab. 3 summarizes simulated SLLs and QLLs for all steering angles of 15°, 30°, and 45° across the 137–142 GHz range. Most cases maintain QLLs and SLLs consistently below -10 dB, except the SLL of the

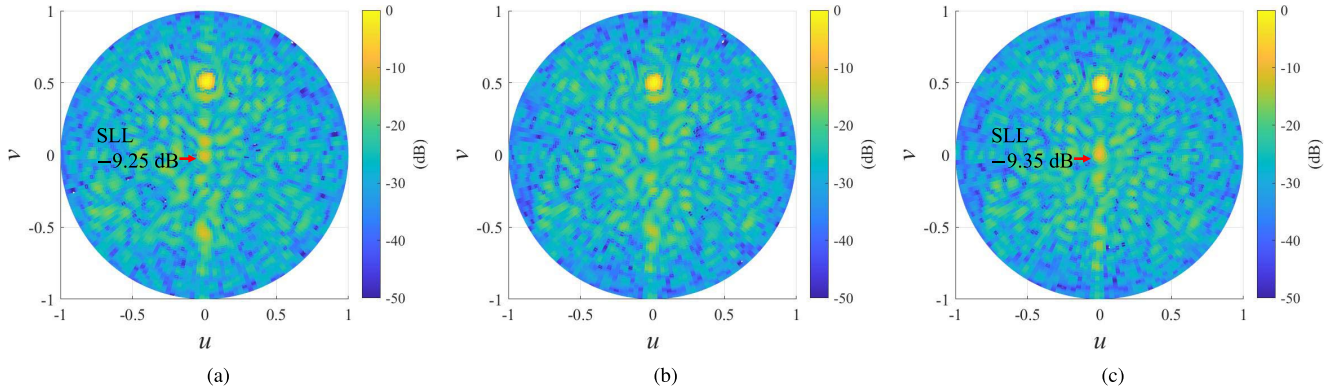

FIGURE 9. Simulated *u*–*v* plane radiation patterns for the EMS at a steering angle of 30° at (a) 137 GHz, (b) 140 GHz, and (c) 142 GHz.

TABLE 3. Simulated SLL and QLL of the EMS for different beam-steering angles.

Freq. (GHz)	15°		30°		45°	
	SLL (dB)	QLL (dB)	SLL (dB)	QLL (dB)	SLL (dB)	QLL (dB)
137	−9.57	−14.31	−9.25	−11.05	−8.64	−12.11
140	−10.08	−15.17	−13.05	−13.05	−11.16	−11.89
142	−11.51	−15.03	−9.35	−13.11	−7.24	−12.00

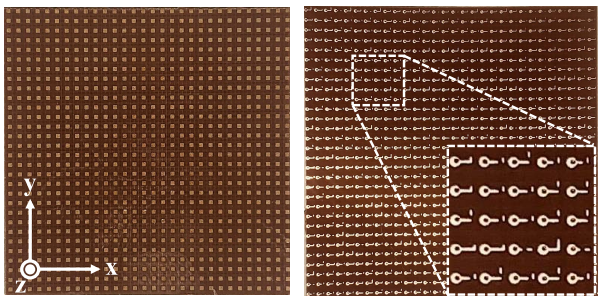

FIGURE 10. Photograph images of the manufactured MASB: (a) Top patches and (b) TX lines.

45° case, confirming stable suppression of quantization lobes over 5 GHz. These results demonstrate that the MASB EMS preserves beam directionality and effectively suppresses sidelobes and quantization lobes across the wide bandwidth.

As regards the computational efficiency of the derived synthesis methodology, it is also worth remarking that the entire optimization process aimed at the configuration of $P \times Q = 900$ discrete variables and $P \times Q \times N = 2700$ binary variables required less than 40 minutes on a standard laptop PC equipped with a single-core 1.60 GHz CPU and running a non-optimized MATLAB implementation of the method. Such a result demonstrates the scalability of the proposed strategy and its applicability to wide-aperture RP-EMS architectures (e.g., including hundreds/thousands of MAs).

IV. MEASUREMENT RESULTS

A. MASB EMS FABRICATION

Three MASB EMSs steering at $\widehat{\theta^n} = 15°$, 30°, and 45° on the $\varphi_r = 90°$ operating at plane at 140 GHz were fabricated. The MASB EMSs possess optimized non-periodic phase distributions of C^{opt}, enabled by 180Â° phase control with only 1-bit control, thus steering the normally incident plane wave towards desired directions while suppressing QLL and SLL. Fig. 10(a) and (b) show photographed top views of two TLY-5 substrates with 30 × 30 patches and Tx lines, respectively, before bonding each other. Both layers then were bonded using two Taconic bond layers to form final MASB EMSs. The final dimensions of the fabricated MASB EMSs were 3.14 × 3.14 cm^2 (15λ × 15λ).

B. MEASUREMENT RESULTS

Fabricated MASB EMSs were measured in an antenna radiation pattern measurement setup using reference TX and RX horn antennas, and its schematic is shown in Fig. 11(a). The MASB EMS was installed at the center of the motorized rotator, and a transmitting (TX) antenna faced the MASB EMS at a 35 cm (163λ) distance on the same platform to ensure the normal plane wave incidence scenario. The receiving (RX) antenna was also fixed 125 cm (584λ) far from the MASB EMS. During the rotation, the apertures of the TX and RX horn antennas always faced the center of the MASB EMS. The coordinate system in the schematic follows the one used for designing the MASB EMS where the x-y plane is on the surface of the MASB EMS and the origin is the center of the MASB EMS. Since the MASB EMS operates with x-polarized excitation, TX and RX horn antennas are configured for x-polarization. For the radiation pattern measurement, the rotator with the MASB EMS and TX antenna was rotated from −90° to 90° of θ on the *y*-z plane.

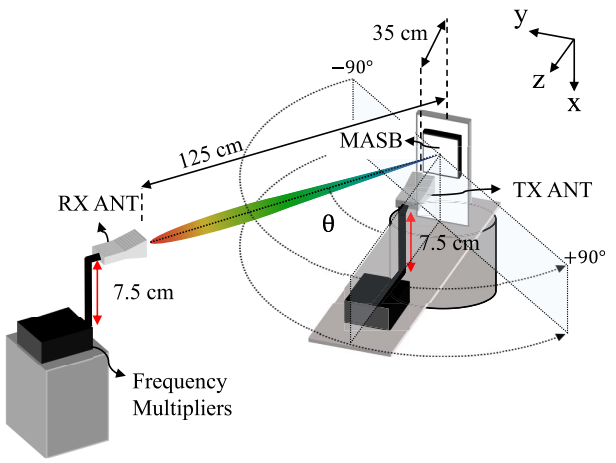

(a)

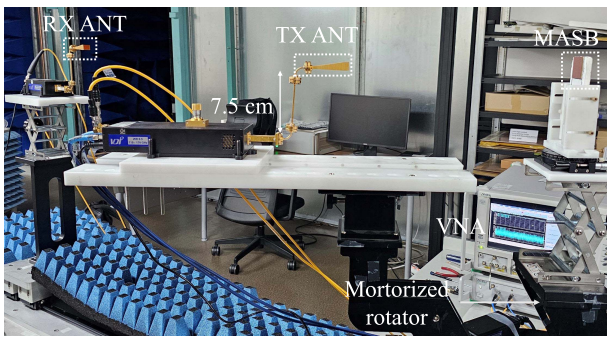

(b)

FIGURE 11. (a) Schematic of the measurement setup for the fabricated MASB EMS and (b) a photograph of the measurement setup.

As shown in a photograph of the measurement setup in Fig. 11(b), the reflective power from the MASB EMS was measured using an Anritsu MS4647B vector network analyzer (VNA) and a 3739C test set from 120 to 160 GHz with 401 data points. A time gating technique was applied in the measurement using a 0.65 ns-wide gating window, set between 5.45 ns and 6.1 ns when the reflection from the MASB EMS occurs. To minimize the shaded area of the multiplier connected to the TX antenna, the height of the TX and RX antennas was increased by 7.5 cm using a bent waveguide. Therefore, a blockage range was reduced from $-3°$ to $3°$ of θ.

The measured normalized S_{21} contour plots of three MASB EMSs at each steering angle depending on θ and frequency (120–160 GHz) were plotted in Fig. 12. The maximum S_{21} points were located at the desired θ values with only minor frequency shifts at 140.5 GHz, 139.2 GHz, and 138.3 GHz for $\widehat{\theta^n} = 15°$, $30°$, and $45°$, respectively.

For more detail, Fig. 13 presents cut views of Fig. 12 in a fixed θ crossing maximum points and compares those with respective simulated S_{21} responses in the frequency domain from three MASB EMSs. The measured data confirms slight shifts of -0.5 GHz, -1.8 GHz, and -1.7 GHz compared to

TABLE 4. Measured QLL reduction and SLL.

Reflection Angle (°)	QLL Reduction (dB)	SLL (dB)
15°	−16.55	−10.07
30°	−12.46	−8.30
45°	−10.84	−10.76

peak points from full-wave simulations for $\widehat{\theta^n} = 15°$, $30°$, and $45°$, respectively. Here, the simulation results have peak points at 141 GHz for both $\widehat{\theta^n} = 15°$ and $30°$, and the $\widehat{\theta^n} = 45°$ case shows the maximum at 140 GHz. In addition, the 3-dB bandwidths were observed to be 15.5 GHz, 10.9 GHz, and 8.9 GHz for $\widehat{\theta^n} = 15°$, $30°$, and $45°$, respectively, corresponding to fractional bandwidths of 11.07%, 7.79%, and 6.36%. This indicates that the EMS's operation is not limited to a single frequency, but a wide bandwidth around 140 GHz. Performance degradation at higher angles is attributed to angular dispersion, as expected for wide-angle beam steering. Overall, the reflection angle, frequency response, and bandwidth at all steering angles were well aligned with the simulation results. Slight discrepancies between the simulation and measurement results could come from minor deviations in metallic patterns, the thickness of the bonding layer, and the dielectric constant in the fabricated MASB EMS structure. In conclusion, the close alignment of the measured and simulated results reinforces the robustness of the MASB design in maintaining effective beam steering across such a high-frequency spectrum over 100 GHz.

Finally, Fig. 14 presents the measured radiation patterns of designed MASB EMSs for $\widehat{\theta_r^n} = 15°$, $30°$, and $45°$ at each S_{21} peak where the signal level is normalized to the case of $\widehat{\theta^n} = 15°$. As noted in Fig. 12, each pattern for $\widehat{\theta^n} = 15°$, $30°$, and $45°$ was captured at 140.5 GHz, 139.2 GHz, and 138.3 GHz, respectively. The decrease in QLL, measured from the local maximum values in the opposite direction of the main beam ($\widehat{\theta^n}$), was observed as -16.55 dB at $\theta = -15°$, -12.46 dB at $\theta = -34°$, and -10.84 dB at $\theta = -46°$. The SLL from three steering angles was also effectively suppressed under -10 dB, with -10.07 dB and -10.76 dB from $\widehat{\theta^n} = 15°$ and $45°$, respectively, except for a slightly increased SLL of -8.3 dB for $\widehat{\theta^n} = 30°$ case. All the measured QLL and SLL are summarized in Tab. 4. These results indicate the MASB EMS's capability to maintain consistent and controlled radiation patterns across different angles, showcasing the effectiveness of the design in minimizing undesired QLL and SLL. The robustness of the performance of the fabricated MASB EMSs is attributed to effective coupling reduction between unit cells and phase linearization addressing manufacturing tolerances.

C. COMPARISON OF 1-BIT REFLECTIVE EMS AND RIS

Recent reflective EMS and RIS operating at millimeter-wave frequencies and employing 1-bit control for reducing QLL and SLL under plane-wave incidence are compared in Tab. 5. Previous studies have predominantly employed

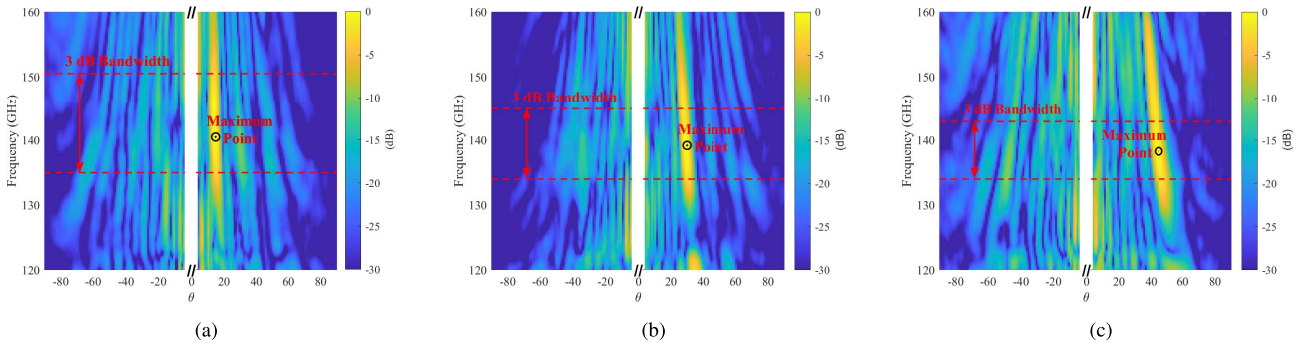

FIGURE 12. (a) Measured normalized S_{21} contour plot of three MASB EMSs depending on θ and frequency for $\hat{\theta}^n = 15°$, (b) $\hat{\theta}^n = 30°$, and (c) $\hat{\theta}^n = 45°$, showing the power distribution normalized to the maximum power at each respective angle.

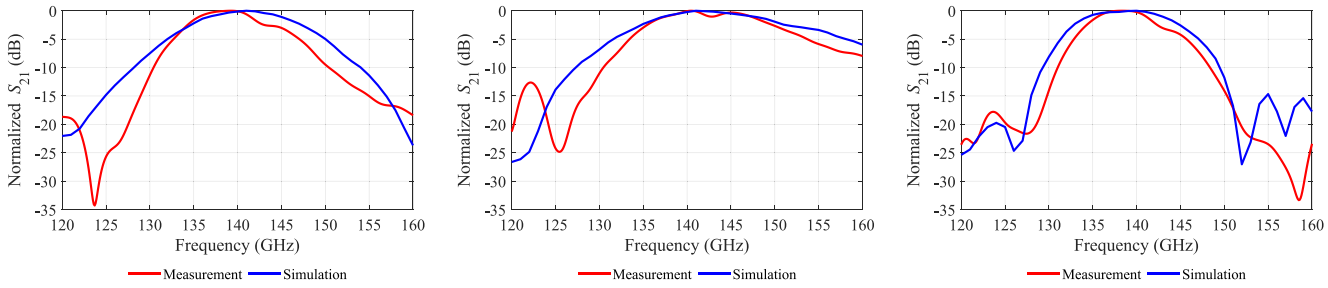

FIGURE 13. Normalized simulation and measurement S_{21} versus frequency for bandwidth at (a) $\widehat{\theta^n} = 15°$, (b) $\widehat{\theta^n} = 30°$, and (c) $\widehat{\theta^n} = 45°$.

TABLE 5. Comparison of 1-bit reflective EMS/RIS at millimeter-wave frequencies for QLL and SLL suppression.

Ref.	Freq. (GHz)	# of Bit Control	Method for QLL/SLL Suppression	Unit Cell Search Method	# of Unit Cell	Periodicity	Switching Method	Beam Directions (°)	3-dB Gain BW (%)
[12]	39	1-bit	Pre-phase	Random	20 × 20	0.5λ	Passive	15, 30	N.A.
[13]	222.5	1-bit	Pre-phase	Random	30 × 30	0.5λ	Passive	−30	3.8
[14]	39	1-bit	Pre-phase	Random	20 × 20	0.52λ	Passive	−15, 15, 30	N.A.
[15]	140	1-bit	Pre-phase	Random	30 × 30	0.5λ	Passive	15, 30, 45	12.64, 9.28, 6.43
This work	140	1-bit	MASB Units	Integer-Coded Evolutionary Algorithm	30 × 30	0.5λ	Passive	15, 30, 45	11.07, 7.79, 6.36

the pre-phase technique based on random phase search using array factor calculation [12], [13], [14], [15]. This study is the first to address the issues of 1-bit reflective EMS by introducing Multi-Atom Single-Bit (MASB) units. Furthermore, the surface current distribution, rather than the phase for a given reflection scenario, was determined using an optimization technique based on an Integer-Coded Evolutionary Algorithm. All the previous studies including this work used passive switching methods instead of diodes due to the scarcity of off-the-shelf components operating at such high frequencies. The effectiveness of the optimization method was validated through a fabricated prototype of a large-aperture metasurface (30 × 30 units) with 0.5λ periodicity operating at 140 GHz, demonstrating suppression of QLL and SLL for multiple reflection angles of 15°, 30°, and 45°. In addition, a measured 3-dB gain bandwidth up to ∼ 11% demonstrates wideband operation, on par with or better than prior works.

V. CONCLUSION

This work introduced a 1-bit reconfigurable EMS concept that mitigates the periodic quantization errors of conventional 1-bit designs—thereby suppressing the undesired quantization lobe. The proposed synthesis procedure employs an integer-coded evolutionary algorithm to jointly optimize the MA reflection phases with a 45° spacing and their 1-bit electronic states (ON/OFF). Under normal incidence, the optimized aperiodic 30 × 30 arrangement supports accurate beam shaping toward 15°, 30°, and 45° using the same physical layout; only the 1-bit switching pattern is changed to select the reflection angle.

For implementation, an aperture-coupled, patch-based MA topology providing a 45° reflection-phase difference and passive 1-bit phase control in the transmission line was adopted to maintain high phase linearity in the 140 GHz band. Measurements on the fabricated EMS confirmed low QLLs of −16.55 dB, −12.46 dB, and −10.84 dB for

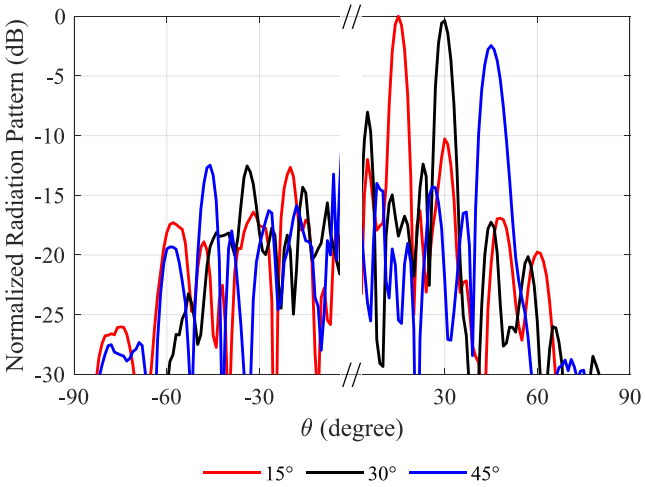

FIGURE 14. Measured radiation patterns for $\hat{\theta}^n = 15^\circ$ at 140.5 GHz, $\hat{\theta}^n = 30^\circ$ at 139.2 GHz, and $\hat{\theta}^n = 45^\circ$ at 138.3 GHz under normal incidence, with each pattern measured at its respective peak S_{21} value.

15°, 30°, and 45° steering, respectively, with the SLL consistently below −10 dB. The prototype further achieved an approximate 11% 3-dB gain bandwidth and reflection efficiency exceeding 15% around 140 GHz. Overall, the results validate the efficacy of the aperiodic, 1-bit EMS paradigm designed via joint optimization of MA reflection phases and 1-bit states, enabling low-quantization-lobe, wide-angle beam reflection with manufacturable hardware.

Future work, beyond the scope of the current paper, will involve implementing of a reconfigurable RIS at 140 GHz using switching ICs. The proposed MASB concept may also be extended to other operative bands and wave manipulation functionalities.

REFERENCES

[1] A. Massa et al., "Designing smart electromagnetic environments for next-generation wireless communications," *Telecom*, vol. 2, no. 2, pp. 213–221, 2021.
[2] G. Oliveri, P. Rocca, M. Salucci, D. Erricolo, and A. Massa, "Multi-scale single-bit RP-EMS synthesis for advanced propagation manipulation through system-by-design," *IEEE Trans. Antennas Propag.*, vol. 70, no. 10, pp. 8809–8824, Oct. 2022.
[3] P. Rocca et al., "On the design of modular reflecting EM skins for enhanced urban wireless coverage," *IEEE Trans. Antennas Propag.*, vol. 70, no. 10, pp. 8771–8784, Oct. 2022.
[4] A. Benoni, M. Salucci, G. Oliveri, P. Rocca, B. Li, and A. Massa, "Planning of EM skins for improved quality-of-service in urban areas," *IEEE Trans. Antennas Propag.*, vol. 70, no. 10, pp. 8849–8862, Oct. 2022.
[5] C. Liu, F. Yang, S. Xu, and M. Li, "Reconfigurable metasurface: A systematic categorization and recent advances," *Electromagn. Sci.*, vol. 1, no. 4, pp. 1–23, 2023.
[6] F. Yang and Y. Rahmat-Samii, *Surface Electromagnetics: With Applications in Antenna, Microwave, and Optical Engineering*. Cambridge, U.K.: Cambridge Univ. Press, 2019.
[7] F. Wu, R. Lu, J. Wang, Z. H. Jiang, W. Hong, and K.-M. Luk, "A circularly polarized 1 bit electronically reconfigurable reflectarray based on electromagnetic element rotation," *IEEE Trans. Antennas Propag.*, vol. 69, no. 9, pp. 5585–5595, Sep. 2021.
[8] G. Li, J. Han, X. Ma, X. Wang, H. Liu, and L. Li, "A simplified, double-layer and low-profile 1-bit reconfigurable reflectarray for 2-D space-time beam steering," *IEEE Antennas Wireless Propag. Lett.*, vol. 23, no. 2, pp. 658–662, Feb. 2024.
[9] S.-G. Zhou et al., "A wideband 1-bit reconfigurable reflectarray antenna at Ku-band," *IEEE Antennas Wireless Propag. Lett.*, vol. 21, no. 3, pp. 566–570, Mar. 2022.
[10] H. Yang et al., "A 1-bit 10 × 10 reconfigurable reflectarray antenna: Design, optimization, and experiment," *IEEE Trans. Antennas Propag.*, vol. 64, no. 6, pp. 2246–2254, Jun. 2016.
[11] H. Yang et al., "A study of phase quantization effects for reconfigurable reflectarray antennas," *IEEE Antennas Wireless Propag. Lett.*, vol. 16, pp. 302–305, 2016.
[12] J. Yin, Q. Wu, Q. Lou, H. Wang, Z. N. Chen, and W. Hong, "Single-beam 1 bit reflective metasurface using prephased unit cells for normally incident plane waves," *IEEE Trans. Antennas Propag.*, vol. 68, no. 7, pp. 5496–5504, Jul. 2020.
[13] B. G. Kashyap, P. C. Theofanopoulos, Y. Cui, and G. C. Trichopoulos, "Mitigating quantization lobes in mmWave low-bit reconfigurable reflective surfaces," *IEEE Open J. Antennas Propag.*, vol. 1, pp. 604–614, 2020.
[14] Q. Wu, X. Long, J. Yin, C. Yu, H. Wang, and W. Hong, "Single-layer 1-bit prephased single-beam metasurface using true-time delayed unit cells," *IEEE Antennas Wireless Propag. Lett.*, vol. 21, no. 6, pp. 1095–1099, Jun. 2022.
[15] T. Kim, S. Lee, J. Kim, S. Oh, J. Oh, and S. Choi, "Pre-phased 1-bit reflective passive metasurface with optimum number of pre-phasing for low QLL and SLL at 140 GHz," *IEEE Trans. Antennas Propag.*, vol. 73, no. 2, pp. 975–985, Feb. 2025.
[16] G. Oliveri, M. Salucci, and A. Massa, "Features and potentialities of static passive EM skins for NLOS specular wireless links," *IEEE Trans. Antennas Propag.*, vol. 71, no. 10, pp. 8048–8060, Oct. 2023.
[17] G. Oliveri, F. Zardi, P. Rocca, M. Salucci, and A. Massa, "Building a smart EM environment—AI-enhanced aperiodic micro-scale design of passive EM skins," *IEEE Trans. Antennas Propag.*, vol. 70, no. 10, pp. 8757–8770, Oct. 2022.
[18] G. Oliveri, P. Rocca, M. Salucci, and A. Massa, "Holographic smart EM skins for advanced beam power shaping in next generation wireless environments," *IEEE J. Multiscale Multiphys. Comput. Techn.*, vol. 6, pp. 171–182, 2021.
[19] P. Rocca, M. Benedetti, M. Donelli, D. Franceschini, and A. Massa, "Evolutionary optimization as applied to inverse scattering problems," *Inverse Problems*, vol. 25, no. 12, Nov. 2009, Art. no. 123003.
[20] G. Oliveri, M. Salucci, and A. Massa, "Generalized analysis and unified design of EM skins," *IEEE Trans. Antennas Propag.*, vol. 71, no. 8, pp. 6579–6592, Aug. 2023.
[21] R. Coccioli, F.-R. Yang, K.-P. Ma, and T. Itoh, "Aperture-coupled patch antenna on UC-PBG substrate," *IEEE Trans. Microw. Theory Techn.*, vol. 47, no. 11, pp. 2123–2130, Nov. 1999.
[22] E. Carrasco, M. Barba, and J. A. Encinar, "Reflectarray element based on aperture-coupled patches with slots and lines of variable length," *IEEE Trans. Antennas Propag.*, vol. 55, no. 3, pp. 820–825, Mar. 2007.
[23] J. Huang and J. A. Encinar, *Reflectarray Antennas*. Hoboken, NJ, USA: Wiley, 2007.

TAEYOUNG KIM (Member, IEEE) received the B.S. degree in mathematics with a double major in electrical engineering from the University of Ulsan, Ulsan, South Korea, in 2022, and the M.S. degree in electronic and electrical engineering from Kyungpook National University, Daegu, South Korea, in 2024.

He is currently with the R&D Division, Korea Defense Industry, Daejeon, South Korea. His research interests include reconfigurable intelligent metasurfaces for 5G/6G communications.

FRANCESCO ZARDI (Member, IEEE) received the B.Sc. degree in telecommunications and electronic engineering and the M.Sc. degree in information and communications engineering from the University of Trento, Italy, in 2017 and 2019, respectively.

He attended the International Doctoral School in Information and Communication Technology of Trento and is a Senior Researcher with the ELEDIA Research Center. His research activity is mainly focused on electromagnetic diagnostic techniques, the Smart Electromagnetic Environment, and advanced radar architectures.

SANGMIN LEE (Graduate Student Member, IEEE) received the B.S. degree from the Department of Electrical Engineering, University of Ulsan, Ulsan, South Korea, in 2021, and the M.S. degree from the School of Electronic and Electrical Engineering, Kyungpook National University, Daegu, South Korea, in 2024, where he is currently pursuing the Ph.D. degree.

His research interests include millimeter-wave microstrip antenna arrays for radar systems and reconfigurable intelligent metasurfaces for 5G/6G communications.

JINHYUN KIM (Graduate Student Member, IEEE) received the B.S. degree in electrical engineering from Hanyang University, Ansan, South Korea, in 2019. He is currently pursuing the integrated master's and Ph.D. degrees with Seoul National University, Seoul, South Korea.

His research interests include design of microwave integrated circuits and systems for 5G communications and brain stimulation.

UICHAN PARK (Graduate Student Member, IEEE) received the B.S. degree in electronic and electrical engineering from Sungkyunkwan University, Suwon, South Korea, in 2020. He is currently pursuing the integrated master's and Ph.D. degrees with the Department of Electrical and Computer Engineering, Seoul National University, Seoul, South Korea.

His current research interests include digital predistortion for RF power amplifiers, RF/mmWave/microwave integrated circuits, and transmitarray antennas for 5G/6G communication systems.

JUNGSUEK OH (Senior Member, IEEE) received the B.S. and M.S. degrees from Seoul National University, South Korea, in 2002 and 2007, respectively, and the Ph.D. degree from the University of Michigan, Ann Arbor, in 2012.

From 2007 to 2008, he was with Korea Telecom as a Hardware Research Engineer, working on the development of flexible RF device. In 2022, he was a Postdoctoral Research Fellow with the University of Michigan. From 2013 to 2014, he was a Staff RF Engineer with Samsung Research America, Dallas, as a Project Leader of the 5G/Millimeter-Wave Antenna System. From 2015 to 2018, he was a Faculty Member of the Department of Electronic Engineering, Inha University, South Korea. He is currently a Full Professor with the School of Electrical and Computer Engineering, Seoul National University. He has published more than 50 technical techniques, antenna miniaturization for integrated systems, and radio propagation modeling for indoor scenarios.

Prof. Oh was a recipient of the 2011 Rackham Predoctoral Fellowship Award from the University of Michigan, the 2018 SNU Creative-Pioneering Research Award, and the 2019 IEEE AP-S/MTT Seoul Chapter Best Paper Award. He served as a TPC Member and the Session Chair for the IEEE AP-S/USNC-URSI and ISAP. He has been an Associate Editor of *Microwave and Optical Technology Letters* and *ICT Express*.

SANGJO CHOI (Member, IEEE) received the B.S. degrees in electronics engineering from Kyungpook National University, Daegu, South Korea, and in electrical engineering from The University of Texas at Dallas, Dallas, TX, USA, in 2008; and the M.S. and Ph.D. degrees in electrical engineering from the University of Michigan, Ann Arbor, MI, USA, in 2010 and 2014, respectively.

He was with Qualcomm Inc., San Diego, CA, USA, from 2014 to 2017. From 2017 to 2022, he was an Assistant Professor of Electrical Engineering with the University of Ulsan, Ulsan, South Korea. In 2022, he joined the School of Electronics Engineering, Kyungpook National University as an Assistant Professor, where he has been an Associate Professor since 2025. He holds three U.S. patents. His current research interests include beamforming antennas and metasurfaces for 5G/6G systems, nanoantennas for infrared detectors and energy-harvesting devices, and RF packages and modules for wireless communications.

Dr. Choi received Kwanjeong Scholarship form Kwanjeong Education Foundation, South Korea, in 2008. He was a recipient of Honorable Mention and a Finalist from the IEEE International Symposium on Antenna and Propagation Student Paper Competition in 2010 and 2013, respectively.

GIACOMO OLIVERI (Fellow, IEEE) received the B.S. and M.S. degrees in telecommunications engineering and the Ph.D. degree in space sciences and engineering from the University of Genoa, Italy, in 2003, 2005, and 2009, respectively.

He is currently an Associate Professor with the Department of Civil, Environmental, and Mechanical Engineering, University of Trento, and a Board Member of the ELEDIA Research Center. Moreover, he is an Adjunct Professor with CentraleSupélec and a member of the Laboratoire des signaux et systèmes (L2S)@CentraleSupélec, Gif-sur-Yvette, France. He was a Visiting Researcher with L2S in 2012, 2013, and 2015, an Invited Associate Professor with the University of Paris Sud, France, in 2014, and a Visiting Professor with Université Paris-Saclay in 2016 and 2017. He is the author/co-author of over 400 peer reviewed papers on international journals and conferences. His research work is mainly focused on electromagnetic direct and inverse problems, metamaterials analysis and design, and antenna array synthesis.

Dr. Oliveri served as an Associate Editor of the IEEE ANTENNAS AND WIRELESS PROPAGATION LETTERS from 2016 to 2022, and for the IEEE JOURNAL ON MULTISCALE AND MULTIPHYSICS COMPUTATIONAL TECHNIQUES from 2017 to 2023. He is an Associate Editor of *EPJ Applied Metamaterials*, of the INTERNATIONAL JOURNAL OF ANTENNAS AND PROPAGATION, of the INTERNATIONAL JOURNAL OF DISTRIBUTED SENSOR NETWORKS, of the *Microwave Processing*, and of the *Sensors*. He has been serving as the Chair of the AP-S IEEE Press Liaison Committee, as a member of the IEEE AP-S Field Award Subcommittee, and as a member of the IEEE AP-S Membership and Benefit Committee. He is the Chair of the IEEE AP/ED/MTT North Italy Chapter.